Express Polymer Letters Vol.16, No.12 (2022) 1304–1321
Available online at www.expresspolymlett.com
https://doi.org/10.3144/expresspolymlett.2022.94

express polymer letters

Research article

Applying a generic and fast coarse-grained molecular dynamics model to extensively study the mechanical behavior of polymer nanocomposites

Maximilian Ries[*], *Jakob Seibert, Paul Steinmann, Sebastian Pfaller*

Institute of Applied Mechanics, Friedrich-Alexander-Universität, Erlangen-Nürnberg, Germany

Received 14 April 2022; accepted in revised form 9 August 2022

Abstract. The addition of nano-sized filler particles enhances the mechanical performance of polymers. The resulting properties of the polymer nanocomposite depend on a complex interplay of influence factors such as material pairing, filler size, and content, as well as filler-matrix adhesion. As a complement to experimental studies, numerical methods, such as molecular dynamics (MD), facilitate an isolated examination of the individual factors in order to understand their interaction better. However, particle-based simulations are, in general, computationally very expensive, rendering a thorough investigation of nanocomposites' mechanical behavior both expensive and time-consuming. Therefore, this paper presents a fast coarse-grained MD model for a generic nanoparticle-reinforced thermoplastic. First, we examine the matrix and filler phase individually, which exhibit isotropic elasto-viscoplastic and anisotropic elastic behavior, respectively. Based on this, we demonstrate that the effect of filler size, filler content, and filler-matrix adhesion on the stiffness and strength of the nanocomposite corresponds very well with experimental findings in the literature. Consequently, the presented computationally efficient MD model enables the analysis of a generic polymer nanocomposite. In addition to the obtained insights into mechanical behavior, the material characterization provides the basis for a future continuum mechanical description, which bridges the gap to the engineering scale.

Keywords: *mechanical properties, nanocomposites, modelling and simulation, interphase, size effect*

1. Introduction

The properties of polymers can be tailored to meet the increasingly application-specific requirements by adding filler particles. Particularly, nano-sized additives yield considerable gains in optical [1], electrical [2], thermal [3, 4], and mechanical [5] properties. The filler particles influence the characteristics of the matrix polymer in their immediate vicinity [6], creating a region with diverging properties denoted as *interphase* [7]. In the case of non-overlapping interphases, the volume fraction of the interphase is directly proportional to the filler-matrix interface and thus dependent on the surface/volume fraction of the filler particles (at constant filler content). In the case of overlapping interphases, the proportionality depends on the extent of overlaps. Due to their substantial surface-to-volume ratio, nano-sized particles, *i.e.*, one dimension ≤100 nm [8], yield a high interphase volume fraction which affects the overall properties considerably. Consequently, the material behavior of nanocomposites is strongly filler size sensitive, in contrast to conventional (micro)composites [9, 10]. This dependence on the filler size, often called the *size effect*, has been experimentally confirmed in many cases, including calcium carbonate-induced polypropylene [11], magnesium hydroxide-reinforced rubber [12], and ground tire rubber-filled polyethylene [13]. In addition to the filler size,

[*]Corresponding author, e-mail: maximilian.ries@fau.de

the mechanical performance of nanocomposites also depends significantly on the material pairing [14, 15], the filler content, the filler distribution, and the matrix-filler adhesion.

These influence factors affect each other and thus form a complex interaction network which adds to the challenge of experimental investigations. On the one hand, higher filler contents increase the particles' tendency to agglomerate, effectively increasing the filler size [16]. Surface treatment of the nanoparticles, on the other hand, can improve the filler distribution but, in turn, affects the filler-matrix adhesion [17, 18]. Furthermore, the property profiles within the interphase are not experimentally accessible [19]. Therefore, numerical simulations of polymer nanocomposites are required to complement the experiments.

To this end, coarse-grained molecular dynamics (CGMD) is commonly used as it offers a good compromise between molecular resolution and computational cost. In CGMD simulations, individual influence factors can be examined isolated to understand their effects better and thus to be able to implement more accurate models. Odegard and coworkers [20, 21] derived an elastic micromechanics model for nanosilica-reinforced polyimide by matching the continuum's energy to its counterpart in CGMD deformation simulations. Even novel materials can be explored with CGMD, as impressively demonstrated by the work of Moghimikheirabadi and coworkers [22, 23] on the structure and mechanical behavior of ionized polymer nanocomposites. In a previous study on nanosilica-reinforced polystyrene, we used CGMD pseudo-experiments to characterize the mechanical properties of the matrix [24, 25] and filler [26]. Based on these findings, we derived the inelastic property profiles within the interphase via multiscale simulations [27] using a finite element-molecular dynamics coupling method [28, 29]. CGMD facilitated a targeted investigation of the interphase properties as a function of the particle distance at constant volume content and particle radius, which is neither feasible nor measurable experimentally. The employed coarse-grained (CG) model was calibrated via iterative Boltzmann inversion [30] to precisely reproduce the behavior of polystyrene [31, 32]. However, this physically motivated approach leads to highly complex potential formulations, which are computationally expensive and thus limit possible investigations.

Therefore, this paper presents a simple and computationally efficient, generic CG model (Subsection 2.1) suitable for generic studies and method development. We verify the model by extensively analyzing the overall mechanical behavior and demonstrate its capability to reproduce experimentally reported trends (Subsection 3.3). However, contrary to more complex CG models, *e.g.* calibrated via iterative Boltzmann inversion, our model is not capable of accurately reproducing the behavior of one particular thermoplastic. The model is based mainly on Bocharova *et al.* [33], who already proved its applicability to the structure of polymer chains. In particular, their investigations for a blend of long and short polymer chains proved to be in excellent agreement with corresponding experimental results [33]. The present paper first characterizes the two constituents separately: The amorphous matrix polymer behaves elasto-viscoplastic and isotropic (Subsection 3.1), while the crystalline filler exhibits purely elastic but distinctly anisotropic material behavior (Subsection 3.2). In the subsequent thorough analysis of the nanocomposite, which is only feasible with the fast CG model, we investigate the influence of filler size, filler content, and filler-matrix adhesion on the overall material behavior. We reveal that the composite's stiffness (Subsection 3.3.3) and strength (Subsection 3.3.4) increase with higher filler volume and stronger filler-matrix adhesion. In particular, the strength depends considerably on the filler radius, revealing the characteristic size effects for nanocomposites. As a novelty, we obtain an estimation for the thickness of the interphase layer based on the entanglements of the polymer chains (Subsection 3.3.2). Due to the generic nature of the present model, the obtained findings are not applicable to experimental results of one specific matrix-filler combination, but will nonetheless help to gain a better understanding of the mechanical behavior of polymer nanocomposites in general. In our previous MD-based studies of polymer nanocomposites, we focused on a single phase and thus limited the individual investigations to either filler [26], matrix [24, 25, 34], or interphase [27, 35]. On the contrary, this contribution includes a thorough mechanical analysis of both filler and matrix, as well as a detailed study of multi-inclusion composite samples. Overall, the obtained findings demonstrate that, despite its simplicity, the presented model features the mechanical characteristics of a generic thermoplastic nanocomposite and is thus well-suited for future investigations.

2. Model and simulation details

In this contribution, we investigate a generic polymer nanocomposite. Spherical particles with crystalline microstructure (Figure 1c) are embedded into an amorphous polymer without crosslinks, *i.e.*, a thermoplastic (Figure 1d). We vary the filler content and size as visualized in Figures 1a and 1b.

This section introduces the coarse-grained molecular dynamics model (Subsection 2.1) and the investigated samples (Subsection 2.2). Furthermore, we discuss the applied material characterization strategy (Subsection 2.3) and the quantities obtained during the simulations (Subsection 2.4).

Simulation software and data

The MD calculations were performed with LAMMPS (version 29 Oct 2020) [36], while the parameter identification of the continuum mechanical models was done in Matlab. We would also like to acknowledge the usefulness of VMD [83] and its TopoTools [84] and PBCtools (github.com/frobnitzem/pbctools) plugins in the visualisation of our systems. We provide the data published in this contribution via Zenodo [38].

2.1. Coarse-grained potentials for filler and matrix

Normalized units

All quantities are expressed as multiples of the fundamental mass $\bar{m}$, length $\bar{\varsigma}$ (the usual symbol 'σ' is not used here to avoid confusion with the Cauchy stress σ), and energy $\bar{\epsilon}$ as well as the Boltzmann constant k_B and are thus unitless. By choosing these three properties as a base, the fundamental time $\bar{\tau}$ has to fulfill the relation $\bar{\tau} = \sqrt{\bar{m}\bar{\varsigma}^2/\bar{\epsilon}}$.

Without loss of generality, the fundamental quantities are set to 1; thus, $\bar{m} = \bar{\varsigma} = \bar{\epsilon} = 1$ [36]. The fundamental quantities are omitted in this work for better readability, and only the normalized values are given. Consequently, the temperatures T and pressures p discussed below are normalized to the characteristic temperature $\bar{T} = \bar{\epsilon}/k_B$ and the characteristic pressure $\bar{p} = \bar{\epsilon}/\bar{\varsigma}^3$, respectively. Bocharova *et al*. [33] demonstrated that trends obtained by simulation, *e.g.*, the ratio of the gyration radii of two system configurations, were in excellent agreement with their experimental findings on poly(2-vinylpyridine)-silica nanocomposites. Therefore, the normalized units are ideally suited for our goal of showing that the present model is capable of capturing general trends of polymer nanocomposites.

Coarse-grained potentials

We investigate our systems in coarse-grained resolution, which means that so-called superatoms substitute groups of atoms to reduce the computational effort (see, *e.g.*, Müller-Plathe *et al*. [37]). The coarse-grained model has been adopted from Bocharova *et al*. [33]: The matrix-matrix interaction comprises bond, angle, and pair contributions, while the matrix-filler interaction is modeled solely by pair potentials; hence, the polymer chains are not grafted to the nanofillers. Thus, we use the parameters of Bocharova *et al*. [33] for matrix-matrix and matrix-filler interactions (cf. Table 1). Please note that this simple model does not feature dihedral interactions. Bocharova *et al*. [33] have used the same potentials for matrix-matrix and filler-filler interactions since

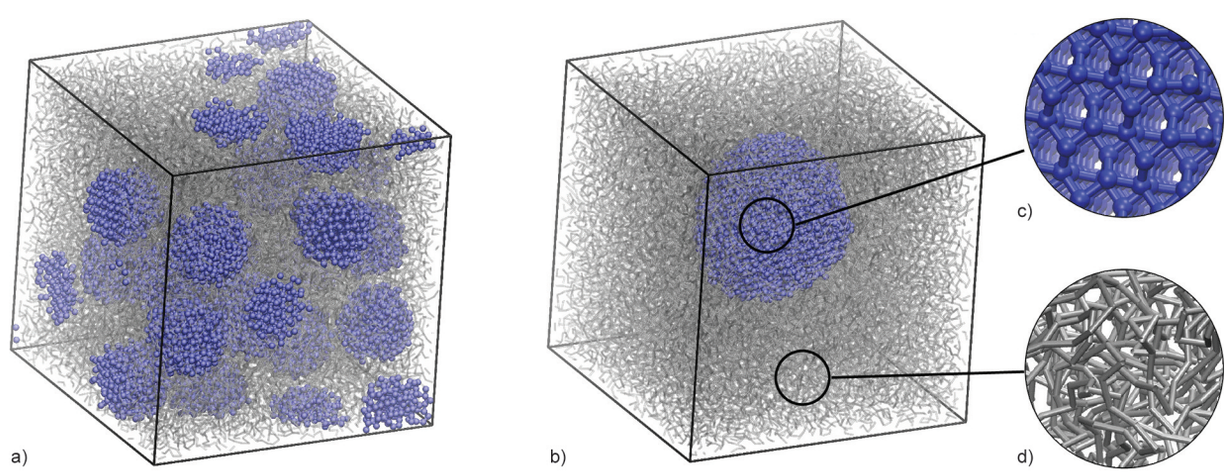

Figure 1. Simulation setup: polymer nanocomposite under periodic boundary conditions for a) 20 filler particles (filler radius $r^{NP} = 4.6$ and filler content $\phi^{NP} = 23.5$ vol%) and b) one filler particle ($r^{NP} = 9.1$ and $\phi^{NP} = 10.3$ vol%); Magnifications highlight crystalline and amorphous microstructures of filler (c) and polymer (d), respectively.

Table 1. Coarse-grained interaction potentials: Bond, angle, and pair interaction potentials and their parameters for filler-filler, matrix-matrix, and matrix-filler interactions using harmonic, finite-extensible nonlinear-elastic (FENE) [41], cosine, and 12/6 Lennard-Jones (LJ) formulations; Equations given in supplementary material [38].

	Bond	**Angle**	**Pair**
Filler-filler (adapted from [33])	harmonic	cosine	LJ
	$K = 3000.0$	$K = 100.0$	$\epsilon = 1.0$
	$r_0 = 0.89$		$\varsigma = 1.0$
			$r_c = \sqrt[6]{2}$
Matrix-matrix (from [33])	FENE	cosine	LJ
	$K = 30.0$	$K = 0.75$	$\epsilon = 1.0$
	$R_0 = 1.5$		$\varsigma = 1.0$
	$\epsilon = 1.0$		$r_c = 2.5$
	$\varsigma = 1.0$		
Matrix-filler (from [33])	–	–	LJ
			$\epsilon^{m-f} = 1.0\|4.0\|8.0$
			$\varsigma = 1.0$
			$r_c = 2.5$

they were mainly interested in the composite's microstructure. Since we focus on the mechanical behavior, we have to adjust the filler-filler interactions to achieve a sufficiently high ratio of filler-to-matrix stiffness, similar to those of real composite materials (cf. Subsection 3.2). We, therefore, choose the numerically robust harmonic bond potential with a significantly higher spring constant $K = 3000$, and also increase the stiffness of angular bonds with $K = 100$ (cf. Table 1). We show in Subsection 3.2 that the neat filler still behaves purely elastic, proving the validity of our parameter choice. Additionally, we vary the strength of the matrix-filler interaction ϵ^{m-f} to model different degrees of filler-matrix adhesion. The used potentials and their corresponding parameters are summarized in Table 1. We provide further details in the supplementary material [38]. For all performed simulations, we set the time step $\Delta t = 0.01$ and the coupling times of the applied Nosé-Hoover thermostat [39] and barostat [40] to $t_T = 1.0$ and $t_p = 5.0$, respectively [33].

2.2. Sample generation and initial equilibration

Neat polymer

A self-avoiding random walk algorithm [42] places 200 polymer chains of 200 super atoms each within a cubic, periodic simulation box for the neat polymer samples. The resulting 40 000 beads are initiated at temperature $T = 1.0$ under an isothermal-isobaric ensemble and then equilibrated in three steps: First, we apply a pressure $p = 0.5$, which is reduced linearly to $p = p_{atm} = 0.0$ [33] over 100 000 time steps to accelerate the initial contraction of the simulation box and to ensure a high degree of entanglements. Second, the system is cooled down below its glass transition temperature of $T_g \approx 0.41$ (cf. Subsection 3.1) to $T = 0.3$ in 140 000 time steps. Finally, the system is equilibrated for another 100 000 time steps at $T = 0.3$ and $p = 0.0$.

Neat filler

We use the crystalline microstructure of the coarse-grained silica from Ries *et al*. [26], scale it to suit the potentials employed here, and re-equilibrate the system under periodic boundary conditions. Since the filler particles are only a few nanometers in size, we assume their microstructure to be single crystalline. This assumption simplifies the future constitutive modeling considerably since no complex grain boundary effects, for example, modeled by Spannraft *et al*. [43], have to be accounted for. Since a single crystal features a uniform, homogeneous crystal lattice, a periodic sample is sufficient for an exact representation. In principle, the investigation of just one crystal cell under periodic boundary conditions is enough. However, for the evaluation of the virial stress, which is very sensitive to thermal fluctuations, a sufficiently large sample is necessary. Based on the experience from previous investigations on single crystals [26], we choose a sample size of 1350 superatoms.

Nanocomposite

The nanocomposite samples are generated analogously to the neat polymer: First, 200 polymer chains with 200 superatoms each are placed in a simulation box using the same random walker as above. However, the chains are now placed around randomly arranged cavities, which are slightly larger than the desired filler particles. Next, the nanoparticles are carved out from a large filler system, randomly rotated, and inserted into these cavities. In the resulting composite samples, neither the polymer nor the fillers are in a state of equilibrium, so the equilibration procedure already used for the neat polymer is employed. During the cooling process, the nanoparticles contract slightly due to the interaction with the surrounding matrix and as a result of their free surface. This

Table 2. Nanocomposite samples: Initial and equilibrated filler radii $\tilde{r}^{NP}$ and r^{NP}, number of filler particles n^{NP}, resulting filler contents ϕ^{NP}, and strength of the filler-matrix interaction ϵ^{m-f}.

n^{NP}	$\tilde{r}^{NP}$	r^{NP}	ϵ^{m-f}	ϕ^{NP} [vol%]
8–160	2.5	2.5	8.0	1.3–23.4
1–20	5.0	4.6	1.0-8.0	1.1–18.4
1–5	7.5	6.8	8.0	3.4–15.0
1–2	10.0	9.1	8.0	7.7–14.6

shrinkage is most pronounced for the largest particles considered, with their radius decreasing from $\tilde{r}^{NP} = 10.0$ to $r^{NP} = 9.1$. We investigate filler radii of $r^{NP} = 2.5$ to 9.1 and filler contents ϕ^{NP} from 1.1 to 23.4, as summarized in Table 2. Note that the identification of the interphase thickness in Subsection 3.3.2 requires samples with 1650 chains of length 200 surrounding a single nanoparticle to ensure a sufficiently large simulation box for $\tilde{r}^{NP} = 7.5$.

2.3. Material characterization

Classification strategy

The four paradigmatic material models, *elasticity*, *plasticity*, *viscoelasticity*, and *viscoplasticity*, can be identified by means of two mechanical phenomena: Rate-dependence and quasi-static hysteresis [44]. If the material exhibits an equilibrium hysteresis under quasi-static loading conditions, it behaves plastically. Otherwise, no plasticity is involved [45]. A rate-dependent material response reveals additional viscous components. This categorization strategy depicted in Figure 2a was originally experimentally motivated but is also suitable for molecular dynamics simulations, as was shown in our previous contributions [24, 25, 26].

Applied deformation

In order to capture the complete material behavior, we apply strain-controlled uniaxial and shear deformations, as visualized in Figures 2b and 2c, respectively. The uniaxial deformation is achieved by deforming the simulation box in the tensile direction via a canonical ensemble (NVT). The resulting tensile strain ε_{ii} is calculated as Equation (1):

$$\varepsilon_{ii} = \frac{\ell_i - L_i}{L_i} \tag{1}$$

with initial and current box length L_i and ℓ_i, respectively. The application of the isothermal-isobaric ensemble (NPT) in the transverse directions allows for a free lateral contraction under atmospheric pressure p_{atm}, which is set to zero for the present model [33]. In contrast, simple shear is by definition volume-preserving [47], thus requires only a canonical ensemble (NVT). The applied shear strain ε_{ij} results from Equation (2):

$$\varepsilon_{ij} = \frac{1}{2}\frac{u_i}{L_j} \approx \frac{1}{2}\gamma_{ij} \tag{2}$$

with shear angle γ_{ij}, displacement u_i, and box length L_j. To capture the behavior under loading and unloading the overall strain is imposed for both deformation cases, either time-proportionally or time-periodically specified by Equation (3):

$$\varepsilon_{ij}(t) = \dot{\varepsilon} t \quad \text{and} \quad \varepsilon_{ij}(t) = \varepsilon^a \sin\left(\frac{\dot{\varepsilon}^{max}}{\varepsilon^a} t\right) \qquad i,j \in x,y,z \tag{3}$$

respectively [24, 26]. In the former, the deformation is applied at a constant strain rate $\dot{\varepsilon}$, *i.e.*, linearly

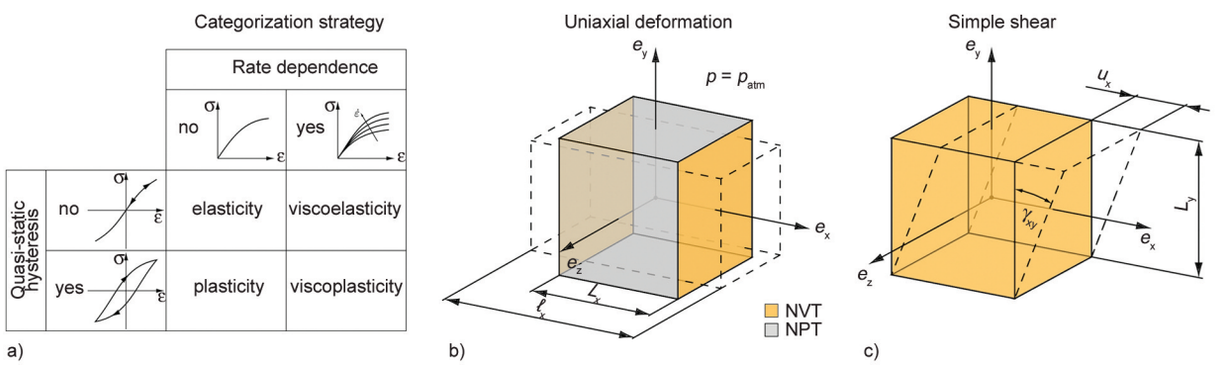

Figure 2. Material characterization: a) classification scheme based on rate dependence and quasi-static hysteresis into elasticity, plasticity, viscoelasticity, and viscoplasticity (from Ries *et al.* [26] , based on Pfaller [46]); strain-controlled deformation via NVT ensemble: b) uniaxial deformation with initial and deformed lengths L_x and ℓ_x, free lateral contraction enabled by NPT ensemble and atmospheric pressure p_{atm}; c) simple shear with length L_y, displacement u_x, and shear angle γ_{xy}.

over time t. In the latter, the strain follows a sinusoidal course with amplitude ε^{a} and maximum strain rate $\dot{\varepsilon}^{max}$.

2.4. Obtained quantities

Stress and derived quantities

In order to measure the stress due to the applied deformation, we evaluate the virial stress tensor σ [48] (Equation (4)):

$$\sigma = -\frac{1}{V}\sum_{i=1}^{n_A}\sum_{\substack{j=1\\ j>i}}^{n_A}\mathbf{f}_{ij}\otimes\left[\mathbf{r}_i-\mathbf{r}_j\right]-\frac{1}{V}\sum_{i=1}^{n_A}m_i\mathbf{v}_i\otimes\mathbf{v}_i \quad (4)$$

whose first term represents the virial contribution with volume V, number of atoms n_A, atom position vectors $\mathbf{r}_i$ and $\mathbf{r}_j$, and pair-wise interaction force $\mathbf{f}_{ij}$. The second term incorporates the particles' mass m_i and velocity $\mathbf{v}_i$ and thus their temperature. According to Subramaniyan and Sun [49], the virial stress tensor σ corresponds to the Cauchy stress tensor commonly used in continuum mechanics. Since the stress observed in a molecular system is typically affected by strong fluctuations, we apply a Savitzky-Golay filter [50] with linear polynomials to smooth them out. From the filtered stress, we derive the following quantities: The stiffness is usually expressed in terms of Young's modulus E, determined here as the secant of the tensile stress at 1% tensile strain. Since polymers often do not exhibit a distinct yield point, we choose the maximum stress σ^{max} occurring at up to 20% strain as a measure of the material's strength.

Radius of gyration

In general, the conformation of the polymer chains is characterized by the radius of gyration R_g or the end-to-end distance R_e. Since R_e and R_g are related via $R_e^2 = 6R_g^2$ for linear ideal chains [51] we focus on the gyration radius. However, a supplemental evaluation of R_e is provided in the supplementary material [38]. The radius of gyration R_g accounts for the distribution of mass of each polymer chain and thus measures the chain's size. According to Rubinstein [51], R_g for each chain is defined as Equation (5):

$$R_g = \left[\frac{1}{N}\sum_{i=1}^{N}\left(\mathbf{r}_i-\mathbf{r}_{com}\right)^2\right]^{1/2} \quad \text{with} \quad \mathbf{r}_{com} = \frac{1}{N}\sum_{i=1}^{N}\mathbf{r}_i \quad (5)$$

with N atoms per chain, the i-th atom's position $\mathbf{r}_i$, and the chain's center of mass $\mathbf{r}_{com}$. To examine its spatial distribution, we average R_g for each chain over 10 000 time steps and associate this mean radius of gyration with the corresponding chain's center of mass $\mathbf{r}_{com}$.

Entanglements

Contrary to studies where the interphase is identified by the end-to-end distance [52] or the radius of gyration of the polymer chains [32, 53], we follow the approach of Moghimikheirabadi *et al.* [54] and examine the nanoparticles' influence on the entanglement network. To this end, we employ the Z1 Algorithm [55–58], which reduces each polymer chain to its primitive path considering the entire polymer network. The resulting 'kinks' Z of the primitive paths can be related to the entanglements of the chains and thus characterize the thermoplastic polymer network. The nanoparticles disturb the equilibration of the chains and are therefore considered as obstacles to the Z1 algorithm ('frozen limit'). In samples containing only one nanoparticle, we can quantify its impact via the density distribution of the kinks $\rho_z(r)$ (Equation (6)):

$$\rho_z(r) = \frac{n_z}{V}\bigg|_{\Omega(r)} \quad (6)$$

with the number of kinks n_z within a hollow sphere $\Omega(r)$ of radius $r > r^{NP}$ and volume V around the nanoparticle's center of mass (cf. Figure 8a inset).

Global Shannon entropy

To evaluate the filler dispersion, we employ the global Shannon entropy χ^{NP} [59]. The idea is to separate the simulation box into a grid of q cuboids and derive the entropy via the observed probability p_i that a filler is found in grid i. The global Shannon entropy χ^{NP} is then computed as Equation (7):

$$\chi^{NP} = -\left[\sum_{i=0}^{q}p_i\log(p_i)\right]\frac{1}{\log(q)} \quad \text{with} \quad p_i = \frac{n_i}{n_{tot}} \quad (7)$$

where n_i and n_{tot} denote the number of fillers in grid i and the total number of fillers, respectively. In the case of complete spatial randomness of the fillers, $p_i = q$ and thus $\chi^{NP} = 1$, while $\chi^{NP} \to 0$ for highly aggregated systems. The global Shannon entropy has been used by Camesasca *et al.* [60] to analyze the mixing quality of polymer blends. Moreover, Kam *et al.* [59] compared 14 commonly used distribution metrics and identified χ^{NP} as the optimal measure for the evaluation of nanocomposites. Based on their

findings, we choose $q = 27$ arranged in a 3×3×3 grid for our studies.

3. Results and discussions

3.1. Neat polymer

In this section, we first consider the mechanical behavior of the neat polymer without filler particles. We identify the glass transition temperature $T_g \approx 0.41$, show the isotropy of the polymer, and reveal that it behaves elasto-viscoplastically.

Glass transition temperature

Bocharova *et al*. [33] studied the polymer in the molten state at temperature $T = 1.0$. However, for the present analysis of the mechanical properties, the polymer has to be cooled down below its glass transition temperature T_g to behave like a solid. Hence, Figure 3a displays the stress-strain curves of uniaxial tensile tests at different temperatures. Clearly, at $T \geq 0.5$, the sample is still in a molten state and thus cannot sustain any tensile stresses. Only at lower temperatures $T \leq 0.4$, the material experiences stresses, with both the initial slope (Young's modulus) and the maximum stresses increasing with decreasing temperature. Consequently, the glass transition occurs between $T = 0.4$ to 0.5, with $T_g \approx 0.41$ derived from the density evolution during quenching (cf. supplementary material [38]). Such a strongly temperature-dependent material behavior is typical for polymers. We choose $T = 0.3$ for all following investigations, which is sufficiently far below T_g, but without suppressing all dynamic effects.

Isotropy

Figure 3b reveals that the mechanical response of the present polymer is independent of the loading direction, *i.e.*, isotropic. This confirms that the polymer chains indeed appear in amorphous form, thus validating our random walk algorithm and subsequent equilibration procedure as introduced in Subsection 2.2. Consequently, we perform all following uniaxial and shear tests for the neat polymer only in *x*- and *xy*-direction, respectively.

Large deformation

The inset in Figure 3b shows that the tensile stress increases almost linearly for strains from 25% up to 100%. This is reasonable since no bond breakage criterion is implemented, which would cause material damage. Hence, the MD model currently provides no meaningful results for such large strains. An extension to include a suitable bond breakage criterion is currently in progress.

Rate dependence

The rate-dependent stress-strain curves due to time-proportional tensile and shear deformation are shown in Figures 4, respectively. For both load cases, the polymer exhibits a pronounced strain rate dependence, revealing viscous material behavior (cf. Figure 2a). This rate dependence is consistent with the previously identified temperature dependence, as both are related by the time-temperature superposition principle [61].

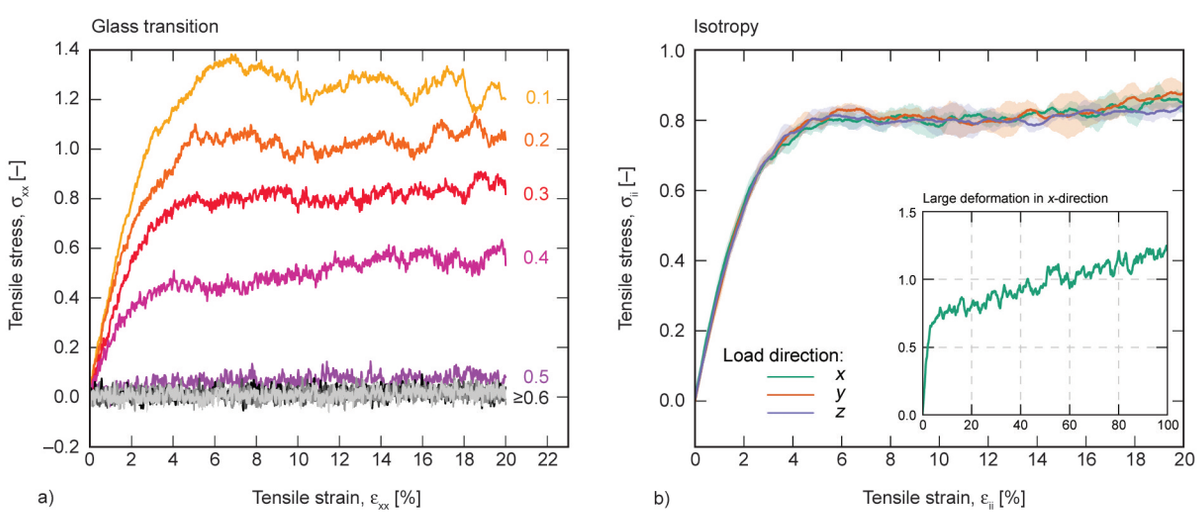

Figure 3. Uniaxial tension test with $\dot{\varepsilon} = 5 \cdot 10^{-5}$: a) temperature dependence with glassy state for $T \leq 0.4$ (1 sample for each temperature); b) isotropic behavior shown by loading in *x*-, *y*-, and *z*-direction (band displays standard deviation over 5 samples); inset: large deformation up to 100%.

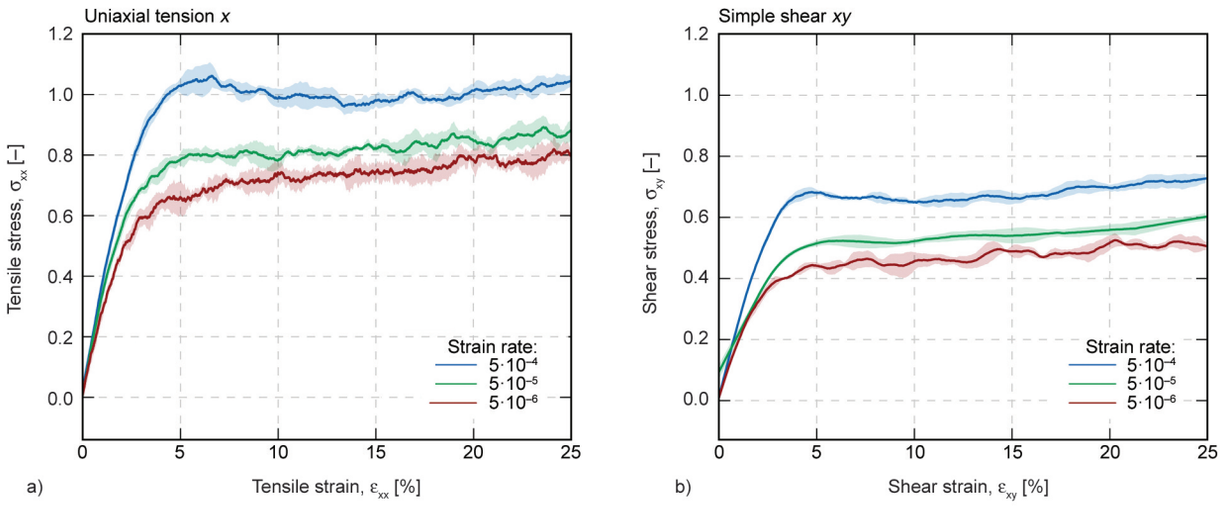

Figure 4. Strain rate dependence: a) uniaxial tension in *x*-direction; b) simple shear in *xy*-direction; Bands display standard deviations over five samples.

Equilibrium hysteresis

Figure 5a displays the stress-strain curves resulting from time-periodic uniaxial deformation for strain amplitudes ε^a from 1 to 20%. It is evident that a stable equilibrium hysteresis is already formed in the first deformation cycle for all amplitudes. The area of the σ–ε-hysteresis increases with larger amplitudes and is proportional to the dissipated energy [62]. The larger dissipation indicates increasingly inelastic material behavior at larger strain amplitudes. An exception to this is $\varepsilon^a = 1\%$: In this case, the area of the hysteresis vanishes, thus, no energy is dissipated, and purely elastic material behavior is observed for such small deformations.

Relaxation

The stress relaxation shown in Figure 5b is performed directly after the fourth load cycle when reaching zero strain and thus reveals whether the observed inelasticity stems from viscous or plastic effects. In this procedure, any remaining stress for $t \to \infty$ would be due to plastic effects, whereas the elastic contributions would vanish immediately, and the viscous contributions would disappear over time. To derive the converged plastic stress, we extrapolate our simulation data with $\sigma_{xx}(t) = [at + b]/[t + c]$, where $a = \sigma_{xx}^{t\to\infty}$ [24]. The stress relaxation in Figure 5b confirms purely elastic behavior for the smallest amplitude and the presence of viscous effects for amplitudes $\varepsilon^a \geq 5\%$. However, the fact that the stress does not vanish completely indicates additional plastic effects. Interestingly, $\sigma_{xx}^{t\to\infty}$ seems to converge to a constant value for $\varepsilon^a \geq 15\%$, as highlighted in the inset of Figure 5b. This implies that only the viscous components increase for larger deformations while the plastic components remain constant, which is

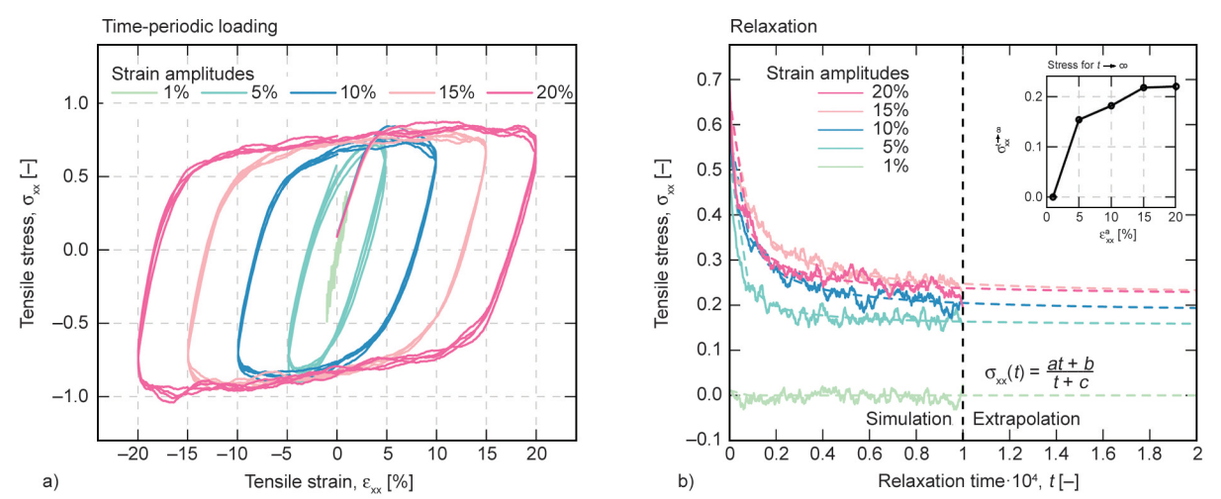

Figure 5. a) Time-periodic loading with 4 sinusoidal cycles with strain amplitudes from 1 to 20%; b) subsequent stress relaxation at the end of the 4th loading cycle; inset: Relaxed stress for $t \to \infty$ derived via extrapolation.

most likely due to the missing damage as discussed above.

Computation time

Finally, we evaluate the computational performance of the present generic MD model. To this end, a comparison to the simulations of polystyrene with a more sophisticated CG model in Bauer *et al.* [63] is suitable since these were carried out on the same hardware using lammps. The generic model stands out in 2 aspects: On the one hand, the computation of the time steps is much more efficient with 180 compared to 90 time steps/s. On the other hand, significantly fewer time steps are required to apply the deformation in the generic model, as shown in Table 3. Of course, the more complex model provides a more accurate representation of the specific behavior of the polymer, which is polystyrene in the present case. However, the model introduced here is much more attractive for generic investigations and method development due to its significantly higher computational efficiency.

Table 3. Computational cost for uniaxial tension tests: Comparison of the present generic model and a sophisticated coarse-grained model of polystyrene [63] at typical strain rates of $\dot{\varepsilon} = 5 \cdot 10^{-5}$ (generic model with dimensionless time) and $\dot{\varepsilon} = 1\% \cdot ns^{-1}$ (polystyrene with physical time), respectively; Both systems comprise 60 000 atoms: Computational efficiency in time steps per walltime, *i.e.* timesteps/s, and load discretization in required timesteps/(1% strain); simulations performed with lammps on the same hardware.

Model	Efficiency $\frac{\text{timestep}}{\text{s}}$	Load discretization $\frac{\text{timestep}}{\text{1\% strain}}$
Generic model	≈ 180	40 000
Polystyrene	≈ 90	800 000

3.2. Neat filler

Next, we focus on the mechanical behavior of the neat filler and show that it behaves purely elastic and is significantly stiffer than the neat polymer. Hence, the filler particles within the composite deform considerably less than the softer polymer matrix. Consequently, an investigation of the material behavior of the filler up to 10 % strain is sufficient for our purposes. Additionally, the filler exhibits pronounced anisotropy due to its crystalline microstructure.

Anisotropy

From the stress-strain curves in Figures 6, it is evident that the filler exhibits pronounced anisotropic behavior for uniaxial tension and simple shear, respectively. This is attributed to the crystalline microstructure of the filler (cf. Figure 1c), which causes the tensile stiffness in the *x*-direction to be significantly higher than in the *y*- and *z*-directions. In addition, the tensile stress in the *x*-direction σ_{xx} increases almost linearly, while σ_{yy} and σ_{zz} follow a distinctly nonlinear, *i.e.* concave path. The shear stresses behave similarly, albeit σ_{yz} is linear, σ_{xy} is slightly concave, and σ_{xz} is significantly lower and slightly convex.

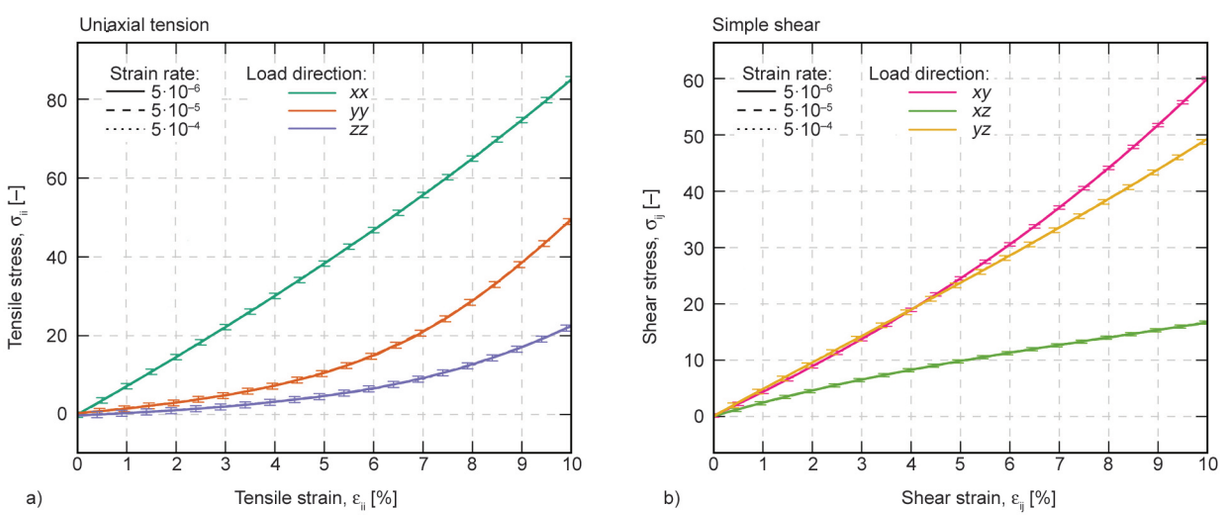

Figure 6. Time-proportional loading at strain rates from $5 \cdot 10^{-6}$ to $5 \cdot 10^{-4}$ (all overlapping) reveals anisotropy and rate-independence for a) uniaxial tension in *x*-, *y*-, and *z*-direction; b) simple shear in *xy*-, *xz*-, and *yz*-direction; Whiskers indicate fluctuations.

Rate independence

The stress-strain curves in Figures 6 for different strain rates perfectly overlap for the individual load directions. Consequently, the filler exhibits no rate dependence and hence no viscosity. Compared to the pure polymer (cf. Figure 4), the filler behaves significantly stiffer, which enables the model composite to capture the generic behavior of a polymer with stiffer inclusions.

Cyclic loading

Due to the stiffness difference, we expect the nanoparticles to deform significantly less than the softer matrix during the loading of the nanocomposite. Therefore, an analysis of the cyclic behavior with strain amplitudes of $\varepsilon^a = 5\%$ is sufficient for the filler. The cyclic load curves in Figure 7 clearly illustrate that no hysteresis develops for the filler, and thus no energy is dissipated. Combined with the observed rate independence, this means that the filler behaves purely elastic with pronounced anisotropy. Furthermore, we observe a tension-compression asymmetry, particularly for loading in *y*-, *z*-, and *xz*-directions.

3.3. Polymer nanocomposite

3.3.1. Experimental trends

In the following, we briefly review the mechanical behavior of polymer nanocomposites reported in experimental studies and derive general trends.

Stiffness

The addition of nanoparticles increases the volume fraction of the stiffer filler phase and, thus also the overall stiffness. As explained above, an additional reinforcement effect occurs for smaller fillers since these cause a larger portion of the stiffer interphase. The stiffness is typically measured as Young's modulus at small deformations, where the matrix-filler adhesion does not yet contribute to the overall behavior [5]. Furthermore, chemical or physical surface modifications introduce additional parameters (grafting agent, grafting density, *etc*.) [64], making the material behavior strongly dependent on the individual material pairing and preparation. Consequently, no general trend can be derived for the influence of matrix-filler adhesion on the nanocomposite's stiffness. In general, the stiffness of nanocomposites

T1) increases with increasing filler content [65–68],
T2) increases with decreasing filler size at constant filler content [67–71], and
T3) shows no clear trend with respect to filler-matrix adhesion (strongly depends on material pairing) [72–74].

Strength

The nanocomposite's strength depends on effective stress transfer between the matrix and filler. Both a larger filler content and smaller nanoparticles increase the filler-matrix interface improving the load transfer and enhancing the strength. In terms of strength, filler-matrix adhesion plays a crucial role: strong adhesion ensures effective loading of the particles and thus high overall strength, while weak filler-matrix interaction results in debonding, which might even weaken the nanocomposite compared to the neat polymer [5]. In general, the strength of nanocomposites

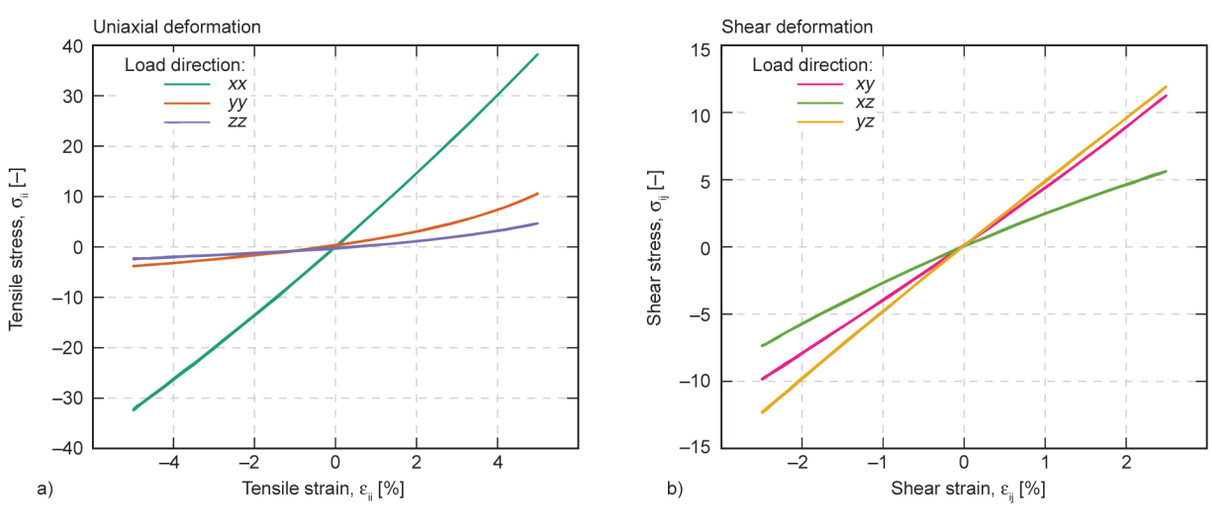

Figure 7. Time-periodic loading indicates pure elasticity with pronounced anisotropy for a) uniaxial deformation in *x*-, *y*-, and *z*-direction with strain amplitude $\varepsilon^a = 5\%$ and b) shear deformation in *x*-, *xz*-, and *yz*-direction with strain amplitude $\varepsilon^a = 2.5\%$; Four sinusoidal loading-unloading cycles (curves overlapping)

T4) increases with increasing filler content [11, 12],
T5) increases with decreasing filler size [6, 12, 75], and
T6) increases with better filler-matrix adhesion [66, 76].

In addition to stiffness and strength, the mechanical performance of nanocomposites is also measured by their fracture toughness. However, the fracture behavior is characterized by large parameter uncertainties [77], and its complex analysis is thus beyond the scope of this contribution.

Filler dispersion

One of the main challenges in the preparation of real polymer nanocomposite specimens is the proper dispersion of the nanofillers [8]. Any remaining filler agglomerate effectively represents a larger particle and thus counteracts the beneficial size effect. Furthermore, these particle clusters represent nuclei for crack initiation and thus have a considerable negative effect on the mechanical properties of the composite. Recently, Petrény *et al*. [78] showed that for poorly dispersed nanofillers strength and stiffness decrease with increasing filler content. However, by adding micro-sized fillers, they enhanced the nanoparticles' dispersion significantly and obtained an increased stiffness for larger filler content at a constant strength. Using a combination of micro- and nano-sized reinforcements to effectively suppress agglomeration and thus facilitate mechanical strengthening has also been reported by Mészáros *et al*. [79]. Consequently, the trends T1) to T7) are only valid for well-dispersed nanoparticles.

3.3.2. Interphase

The interphase denotes the polymer region close to the filler particles in which these induce a modification of the material properties. Such a local effect on the material behavior cannot be measured directly but can be deduced from changes in the microstructure. Therefore, we assess the thickness of the interphase via the entanglement density ρ_z and the radius of gyration R_g. To properly assess the particles' influence, we consider samples with only a single filler particle each. We keep a low filler content of $\phi^{NP} \approx 1$ vol% to ensure that the fillers are surrounded by a sufficient polymer. For statistical validation, the following results are averaged over 20 samples each.

Figure 8a shows the spatial distribution of the entanglement density $\rho_z(r)$ (cf. Equation (6)) normalized to the neat polymer ρ_z^{neat} over the distance from the filler surface d^{NP}. Directly at the particle surface

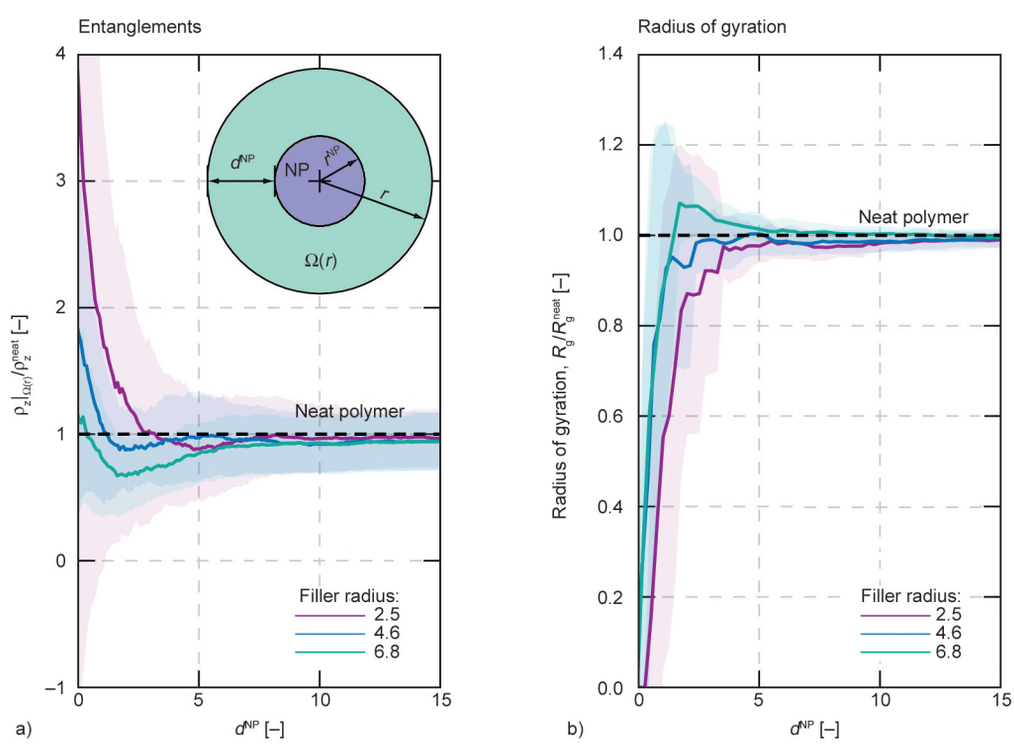

Figure 8. Nanoparticle's effect on the surrounding polymer: Spatial distribution of the entanglement density ρ_z (a) and radius of gyration R_g (b) for filler radius r^{NP} = 4.6 to 6.8, over distance from filler surface d^{NP}, normalized to ρ_z^{neat} and R_g^{neat} of the neat polymer, respectively. Averaged over 20 samples, bands display standard deviation.

($d^{NP} = 0$), we observe an increase in the entanglement density compared to the neat polymer, which is more pronounced for smaller particles. Interestingly, the curves for different r^{NP} differ qualitatively in the range up to $d^{NP} = 5$: For the smallest particle radius $r^{NP} = 2.5$, there is a clear concentration of entanglements near the filler surface. The substantial standard distribution near the filler surface most likely results from the extremely small surface area in the case of small filler particles: In contrast to larger filler particles, only a few polymer beads are located within the considered volume $\Omega(r)$, such that high fluctuations must be expected. A minimum slightly below the neat polymer emerges at $d^{NP} = 5$. With $r^{NP} = 4.6$, a similar minimum already occurs at $d^{NP} \approx 2.2$, *i.e.*, much closer to the particle surface. In contrast, larger particles lead to a much lower minimum at $d^{NP} \approx 2.2$, and thus induce a noticeably lower entanglement density in the vicinity of the filler compared to smaller filler particles. For larger surface distances, all curves converge to the level of the pure polymer, as expected.

Analogously, the spatial distribution of the radius of gyration is displayed in Figure 8b. For all particle sizes, the curves start at 0, since few chains are located in the direct vicinity of the particle surface. In the range $0 < d^{NP} < 5$, the R_g-curves increase and converge towards 1, *i.e.*, the neat polymer. In the same range for d^{NP}, $R_g/R_g^{neat} < 1$ holds only in the case of the smallest particles with $r = 2.5$. Hence, the chains are smaller and more ball-like compared to the neat polymer. Similar results are obtained for $r = 4.6$, albeit the curve exhibits a larger gradient and converges to 1 earlier. A similar gradient is obtained for larger fillers, but $R_g/R_g^{neat} > 1$ occurs, which means that the chains are more stretched out in this area, as compared to the neat polymer. For all particle sizes, the standard deviation over 20 samples is very large near the particle surface but decreases markedly with increasing distance from the filler surface to only ±1% for $d^{NP} > 10$. This indicates that the polymer conformation near the fillers features large local variations, thus requiring statistical validation of the results. The end-to-end distances behave similarly and are therefore only provided in the supplementary material [38].

Figure 8 suggests a correlation between the entanglement density and the radius of gyration: While there are more entanglements and smaller R_g for small fillers, the opposite occurs for larger ones. For all filler sizes, however, the influence of the particles on the surrounding polymer seems to decay at a surface distance $d^{NP} \approx 5$. Consequently, the material properties in this region presumably differ from those of the neat polymer, which implies that the interphase is of thickness 5. However, the filler size-dependent profiles in Figure 8 indicate that the property gradients within the interphase also depend on r^{NP}.

3.3.3. Stiffness

We first consider the overall stiffness, expressed by Young's modulus E normalized to the neat polymer E_{neat}. Figure 9a shows the influence of the filler size on the stiffness for different filler contents ϕ^{NP}. For all radii, the stiffness increases significantly with increasing filler content, consistent with trend T1).

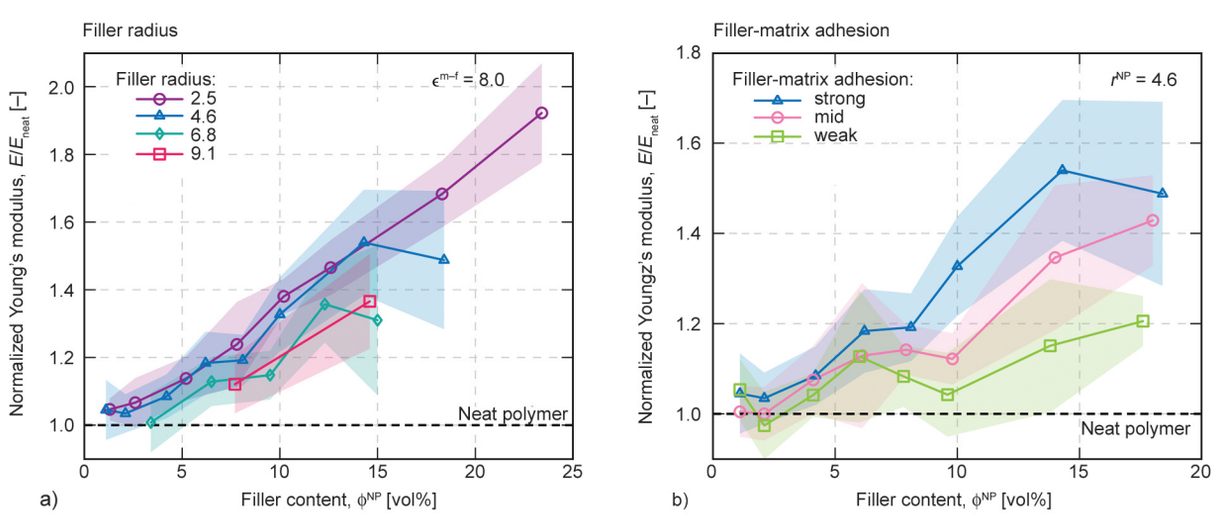

Figure 9. Stiffness of nanocomposite: normalized Young's modulus E/E_{neat} over filler content ϕ^{NP} for a) different filler radii r^{NP} at strong filler-matrix adhesion $\epsilon^{m-f} = 8.0$ and b) filler-matrix adhesion $\epsilon^{m-f} = 8.0$ (strong), 4.0 (mid), and 1.0 (weak) at filler radius $r^{NP} = 4.6$; averaged over 5 samples; bands display the standard deviation for each point.

Furthermore, Young's modulus rises slightly with decreasing particle radius, corresponding to T2), although this is not particularly pronounced.

Figure 9b illustrates the influence of the matrix-filler adhesion over filler content at a particle radius of r^{NP} = 4.6. At low filler contents of $\phi^{NP} < 7$ vol%, the difference between the curves is marginal. For larger ϕ^{NP}, however, it becomes evident that the weaker adhesion of the particles leads to a lower overall stiffness, consistent with T3). This can be attributed to the thinner interphase for weak filler-matrix adhesion, which corresponds to a lower volume fraction of the interphase, which behaves stiffer than the neat polymer.

3.3.4. Strength

Figure 10a presents the strength as maximum stress σ^{max} (cf. Subsection 2.4) normalized to the neat polymer σ^{max}_{neat} *versus* filler content ϕ^{NP} for different filler radii. A higher filler content leads to an increase in strength matching T5). However, this reinforcement is more pronounced for smaller particles and thus in good agreement with T2). A filler content of $\phi^{NP} \approx 15$ vol% already leads to a doubling of the strength with $r = 2.5$, while $r = 9.1$ results in a strengthening of only 40% relative to the neat polymer. In general, the strength exhibits a significantly smaller standard deviation than the stiffness.

Analogously, Figure 10b illuminates the influence of matrix-filler adhesion. Similar to the stiffness, there is no influence of the matrix-filler adhesion at small volume fractions of $\phi^{NP} < 5$ vol%. For larger ϕ^{NP}, weaker adhesion leads to significantly lower strength, as expected from trend T7). While the strength already almost doubles for strong matrix-filler interaction at $\phi^{NP} \approx 18$ vol%, it only improves by 20% for weak adhesion.

3.3.5. Filler dispersion

Since agglomeration of nanoparticles has a crucial impact on the mechanical properties of polymer nanocomposites, we evaluate the degree of dispersion by means of the global Shannon entropy χ^{NP}, given in Equation (7). Since the samples with the smallest fillers (r^{NP} = 2.5) comprise the largest number of nanoparticles (cf. Table 2); they are suited best for evaluating χ^{NP}. Figure 11 depicts the impact of the dispersion on stiffness and strength for r^{NP} = 2.5 and filler contents of $0 < \phi^{NP} < 25$ vol%. On the one hand, χ^{NP} increases with the filler content, and we observe an excellent filler dispersion at high ϕ^{NP}. The significantly lower Shannon entropy for the lowest filler content is attributed to the small number of only eight nanoparticles, which can take a wide range of χ^{NP} starting from their random initial positions. Nevertheless, this verifies our sample generation and equilibration procedure (cf. Subsection 2.2) and confirms that the results of Subsection 3.3.3 and Subsection 3.3.4 have not been distorted by the formation of particle clusters. On the other hand, better dispersion seems to lead to enhanced mechanical properties. However, we also know from Figure 9 and Figure 10 that the filler content ϕ^{NP} improves the

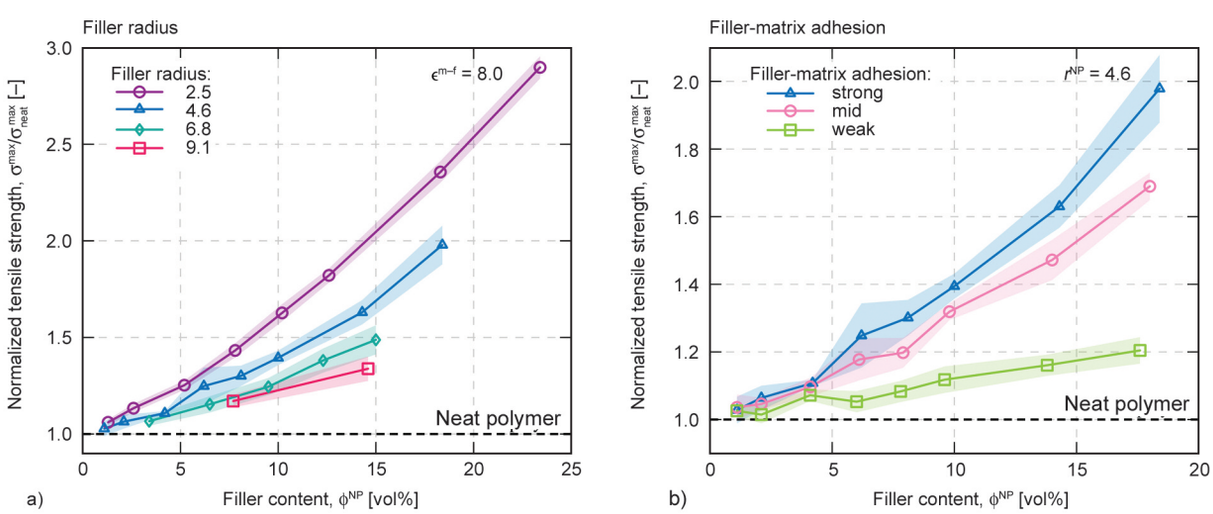

Figure 10. Strength of nanocomposite: normalized maximum tensile stress $\sigma^{max}/\sigma^{max}_{neat}$ over filler content ϕ^{NP} for a) different filler radii r^{NP} at strong filler-matrix adhesion ϵ^{m-f} = 8.0 and b) filler-matrix adhesion ϵ^{m-f} = 8.0 (strong), 4.0 (mid), and 1.0 (weak) at filler radius r^{NP} = 4.6; Bands display standard deviation over 5 samples for each data point.

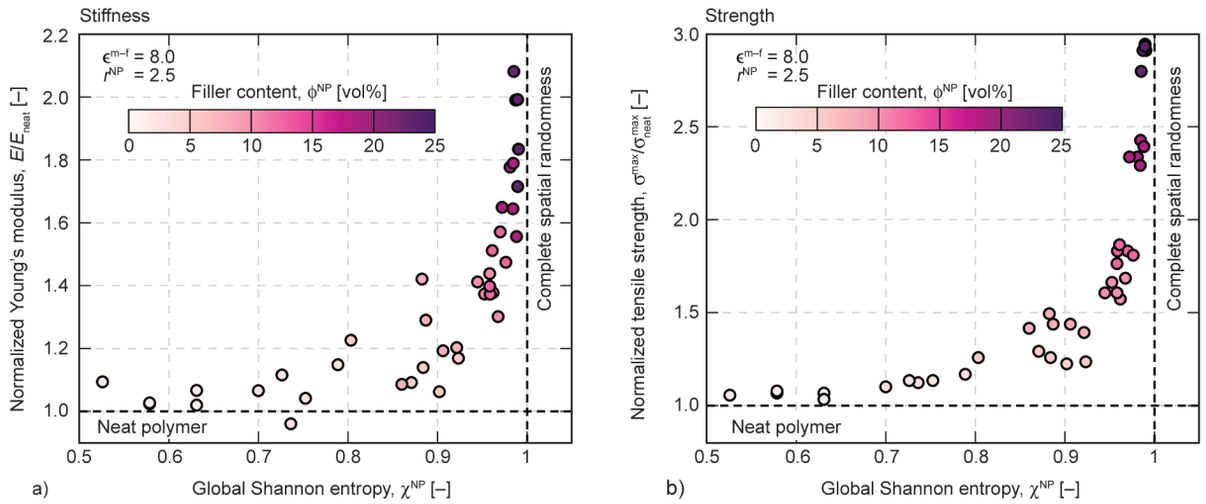

Figure 11. Impact of the particle agglomeration: a) normalized Young's modulus E/E_{neat} and b) normalized maximum tensile stress $\sigma^{max}/\sigma^{max}_{neat}$ over global Shannon entropy χ^{NP} for filler radius $r^{NP} = 2.5$ and strong filler-matrix adhesion $\epsilon^{m-f} = 8.0$; $\chi^{NP} = 1$ at complete spatial randomness of the fillers.

overall stiffness and strength. Therefore, at this point, it is not possible to separate the impact of the filler distribution from one of the filler content. To determine whether agglomeration negatively affects the mechanical properties of our model, MD simulations with enforced particle clusters are required. This, however, exceeds the scope of this work and will be addressed in a future contribution.

3.3.6. Summary

The generic CGMD model presented here is thus capable of reproducing the trends known from experiments for nanocomposites (cf. T1)–T7)). Therefore, it is an excellent tool to facilitate generic studies as well as method development.

4. Conclusions

In this paper, we present a generic and computationally efficient CGMD model for polymer nanocomposite based on Bocharova *et al*. [33]. We first mechanically characterize the neat polymer, which behaves isotropically and elasto-viscoplastically. Subsequently, we show that the neat filler exhibits purely elastic material behavior. However, due to its crystalline microstructure, it displays a pronounced anisotropy. When combined, the polymer and filler represent a generic nanocomposite with spherical filler particles in a softer polymer matrix. We demonstrate that the presented model, despite its simplicity, is able to reproduce the trends for polymer nanocomposites known from experimental studies in the literature. In particular, we observe a strong dependence on the particle size, characteristic of nanocomposites. Furthermore, we prove the presence of an interphase surrounding the nanoparticles and identify its thickness based on the filler-induced changes in the polymer's microstructure. Consequently, the presented model is ideally suited for generic studies and method development, as it is significantly more computationally efficient than more accurate physically motivated CGMD models.

The present study forms the basis for future investigations. In the next step, we intend to calibrate continuum mechanical constitutive laws for polymer and filler analogous to Zhao *et al*. [80] and Ries *et al*. [26] based on the present results. These continuum models are a prerequisite for the identification of the property gradients within the interphase, as described, for example, in our previous studies [27, 35].

To overcome the current limitation of the model in terms of maximum deformation, we will extend it with a suitable bond-breaking criterion. Incorporating this extended CGMD model into an atomistic-to-continuum coupling scheme, such as the recently updated Capriccio method [81, 82] will enable us to unravel the challenging fracture behavior of polymer nanocomposites.

Finally, another extension of the model to investigate also grafted polymer nanocomposites is currently in progress.

Acknowledgements

We sincerely thank Vera Bocharova and Jean Michael Carrillo from the Oak Ridge National Laboratory for kindly sharing the MD force fields on which this work is based. Furthermore, we thank Martin Kröger from ETH Zürich for kindly providing his Z1 algorithm and support for its application. We thank the RRZE of FAU Erlangen-Nürnberg for providing the computational resources for this study.
Sebastian Pfaller is funded by the Deutsche Forschungsgemeinschaft (DFG, German Research Foundation) – 396414850 (Individual Research Grant 'Identifikation von Interphaseneigenschaften in Nanokompositen'). Maximilian Ries, Paul Steinmann, and Sebastian Pfaller are funded by the DFG – 377472739 (Research Training Group GRK 2423 'Fracture across Scales – FRASCAL').

References

[1] Muller O., Hege C., Guerchoux M., Merlat L.: Synthesis, characterization and nonlinear optical properties of polylactide and PMMA based azophloxine nanocomposites for optical limiting applications. Materials Science and Engineering: B, **276**, 115524 (2022). https://doi.org/10.1016/j.mseb.2021.115524

[2] Suematsu K., Arimura M., Uchiyama N., Saita S.: Transparent BaTiO3/PMMA nanocomposite films for display technologies: Facile surface modification approach for $BaTiO_3$ nanoparticles. ACS Applied Nano Materials, **1**, 2430–2437 (2018). https://doi.org/10.1021/acsanm.8b00650

[3] Mortezaei M., Famili M. H. N., Kalaee M. R.: Effect of immobilized interfacial layer on the maximum filler loading of polystyrene/silica nanocomposites. Journal of Reinforced Plastics and Composites, **30**, 593–599 (2011). https://doi.org/10.1177/0731684411399136

[4] Abdolmohammadi S., Siyamak S., Ibrahim N. A., Yunus W. M. Z. W., Rahman M. Z. A., Azizi S., Fatehi A.: Enhancement of mechanical and thermal properties of polycaprolactone/chitosan blend by calcium carbonate nanoparticles. International Journal of Molecular Sciences, **13**, 4508–4522 (2012). https://doi.org/10.3390/ijms13044508

[5] Fu S-Y., Feng X-Q., Lauke B., Mai Y-W.: Effects of particle size, particle/matrix interface adhesion and particle loading on mechanical properties of particulate–polymer composites. Composites Part B: Engineering, **39**, 933–961 (2008). https://doi.org/10.1016/j.compositesb.2008.01.002

[6] Reynaud E., Jouen T., Gauthier C., Vigier G., Varlet J.: Nanofillers in polymeric matrix: A study on silica reinforced pa6. Polymer, **42**, 8759–8768 (2001). https://doi.org/10.1016/S0032-3861(01)00446-3

[7] Vollenberg P., Heikens D.: Particle size dependence of the Young's modulus of filled polymers: 1. Preliminary experiments. Polymer, **30**, 1656–1662 (1989). https://doi.org/10.1016/0032-3861(89)90326-1

[8] Koo J.: Introduction to nanotechnology. in 'Fundamentals, properties, and applications of polymer nanocomposites' (ed.: Koo J. H.) Cambridge University Press, Cambridge, 3–21 (2016). https://doi.org/10.1017/cbo9781139342766.002

[9] Wang M., Berry C., Braden M., Bonfield W.: Young's and shear moduli of ceramic particle filled polyethylene. Journal of Materials Science: Materials in Medicine, **9**, 621–624 (1998). https://doi.org/10.1023/A:1008975323486

[10] Zhu Z-K., Yang Y., Yin J., Qi Z-N.: Preparation and properties of organosoluble polyimide/silica hybrid materials by sol–gel process. Journal of Applied Polymer Science, **73**, 2977–2984 (1999). https://doi.org/10.1002/(SICI)1097-4628(19990929)73:14<2977::AID-APP22>3.0.CO;2-J

[11] Pukánszky B., Vörös G.: Mechanism of interfacial interactions in particulate filled composites. Composite Interfaces, **1**, 411–427 (1993). https://doi.org/10.1163/156855493x00266

[12] Zhang Q., Tian M., Wu Y., Lin G., Zhang L.: Effect of particle size on the properties of $mg(OH)_2$-filled rubber composites. Journal of Applied Polymer Science, **94**, 2341–2346 (2004). https://doi.org/10.1002/app.21037

[13] Kiss L., Simon D. Á., Petrény R., Kocsis D., Bárány T., Mészáros L.: Ground tire rubber filled low-density polyethylene: The effect of particle size. Advanced Industrial and Engineering Polymer Research, **5**, 12–27 (2021). https://doi.org/10.1016/j.aiepr.2021.07.001

[14] Wacharawichanant S., Thongyai S., Phutthaphan A., Eiamsam-ang C.: Effect of particle sizes of zinc oxide on mechanical, thermal and morphological properties of polyoxymethylene/zinc oxide nanocomposites. Polymer Testing, **27**, 971–976 (2008). https://doi.org/10.1016/j.polymertesting.2008.08.012

[15] Wacharawichanant S., Sangkhaphan A., Sa-Nguanwong N., Khamnonwat V., Thongyai S., Praserthdam P.: Effects of particle type on thermal and mechanical properties of polyoxymethylene nanocomposites. Journal of Applied Polymer Science, **123**, 3217–3224 (2011). https://doi.org/10.1002/app.34984

[16] Choi J., Hui C. M., Pietrasik J., Dong H., Matyjaszewski K., Bockstaller M. R.: Toughening fragile matter: Mechanical properties of particle solids assembled from polymer-grafted hybrid particles synthesized by ATRP. Soft Matter, **8**, 4072–4082 (2012). https://doi.org/10.1039/C2SM06915F

[17] Hashemi A., Jouault N., Williams G. A., Zhao D., Cheng K. J., Kysar J. W., Guan Z., Kumar S. K.: Enhanced glassy state mechanical properties of polymer nanocomposites via supramolecular interactions. Nano Letters, **15**, 5465–5471 (2015). https://doi.org/10.1021/acs.nanolett.5b01859

[18] Li G., Zhao T., Zhu P., He Y., Sun R., Lu D., Wong C-P.: Structure-property relationships between microscopic filler surface chemistry and macroscopic rheological, thermo-mechanical, and adhesive performance of SiO_2 filled nanocomposite underfills. Composites Part A: Applied Science and Manufacturing, **118**, 223–234 (2019).
https://doi.org/10.1016/j.compositesa.2018.12.008

[19] Mortezaei M., Farzi G., Kalaee M. R., Zabihpoor M.: Evaluation of interfacial layer properties in the polystyrene/silica nanocomposite. Journal of Applied Polymer Science, **119**, 2039–2047 (2010).
https://doi.org/10.1002/app.32902

[20] Odegard G. M., Gates T. S., Nicholson L. M., Wise K. E.: Equivalent-continuum modeling of nano-structured materials. Composites Science and Technology, **62**, 1869–1880 (2002).
https://doi.org/10.1016/S0266-3538(02)00113-6

[21] Odegard G. M., Clancy T. C., Gates T. S.: Modeling of the mechanical properties of nanoparticle/polymer composites. Polymer, **46**, 553–562 (2005).
https://doi.org/10.1016/j.polymer.2004.11.022

[22] Moghimikheirabadi A., Kröger M., Karatrantos A. V.: Insights from modeling into structure, entanglements, and dynamics in attractive polymer nanocomposites. Soft Matter, **17**, 6362–6373 (2021).
https://doi.org/10.1039/d1sm00683e

[23] Moghimikheirabadi A., Karatrantos A. V., Kröger M.: Ionic polymer nanocomposites subjected to uniaxial extension: A nonequilibrium molecular dynamics study. Polymers, **13**, 4001 (2021).
https://doi.org/10.3390/polym13224001

[24] Ries M., Possart G., Steinmann P., Pfaller S.: Extensive CGMD simulations of atactic PS providing pseudo experimental data to calibrate nonlinear inelastic continuum mechanical constitutive laws. Polymers, **11**, 1824 (2019).
https://doi.org/10.3390/polym11111824

[25] Ries M., Steinmann P., Pfaller S.: Characterization of polystyrene under shear deformation using molecular dynamics. in 'Developments and novel approaches in nonlinear solid body mechanics' (eds.: Abali B. E., Giorgio I.) Springer, Cham, Vol. 130, 219–229 (2020).
https://doi.org/10.1007/978-3-030-50460-1_14

[26] Ries M., Bauer C., Weber F., Steinmann P., Pfaller S.: Characterization of the material behavior and identification of effective elastic moduli based on molecular dynamics simulations of coarse-grained silica. Mathematics and Mechanics of Solids, in press (2022).
https://doi.org/10.1177/10812865221108099

[27] Ries M., Possart G., Steinmann P., Pfaller S.: A coupled MD-FE methodology to characterize mechanical interphases in polymeric nanocomposites. International Journal of Mechanical Sciences, **204**, 106564 (2021).
https://doi.org/10.1016/j.ijmecsci.2021.106564

[28] Pfaller S., Rahimi M., Possart G., Steinmann P., Müller-Plathe F., Böhm M.: An Arlequin-based method to couple molecular dynamics and finite element simulations of amorphous polymers and nanocomposites. Computer Methods in Applied Mechanics and Engineering, **260**, 109–129 (2013).
https://doi.org/10.1016/j.cma.2013.03.006

[29] Pfaller S., Kergaßner A., Steinmann P.: Optimisation of the capriccio method to couple particle- and continuum-based simulations of polymers. Multiscale Science and Engineering, **1**, 318–333 (2019).
https://doi.org/10.1007/s42493-019-00028-y

[30] Reith D., Pütz M., Müller-Plathe F.: Deriving effective mesoscale potentials from atomistic simulations. Journal of Computational Chemistry, **24**, 1624–1636 (2003).
https://doi.org/10.1002/jcc.10307

[31] Qian H-J., Carbone P., Chen X., Karimi-Varzaneh H. A., Müller-Plathe F.: Temperature-transferable coarse-grained potentials for ethylbenzene, polystyrene, and their mixtures. Macromolecules, **41**, 9919–9929 (2008).
https://doi.org/10.1021/ma801910r

[32] Ghanbari A., Ndoro T. V. M., Leroy F., Rahimi M., Böhm M. C., Müller-Plathe F.: Interphase structure in silica-polystyrene nanocomposites: A coarse-grained molecular dynamics study. Macromolecules, **45**, 572–584 (2012).
https://doi.org/10.1021/ma202044e

[33] Bocharova V., Genix A-C., Carrillo J-M. Y., Kumar R., Carroll B., Erwin A., Voylov D., Kisliuk A., Wang Y., Sumpter B. G., Sokolov A. P.: Addition of short polymer chains mechanically reinforces glassy poly(2-vinylpyridine)–silica nanoparticle nanocomposites. ACS Applied Nano Materials, **3**, 3427–3438 (2020).
https://doi.org/10.1021/acsanm.0c00180

[34] Ries M., Weber F., Striegel M., Steinmann P., Pfaller S.: Multiscale FE-MD coupling: Influence of the chain length on the mechanical behavior of coarse-grained polystyrene. in '14th WCCM-ECCOMAS Congress 2020' Vol. 300, 1–12 (2021).
https://doi.org/10.23967/wccm-eccomas.2020.214

[35] Ries M., Weber F., Possart G., Steinmann P., Pfaller S.: A quantitative interphase model for polymer nanocomposites: Verification, validation, and consequences regarding size effects. Composites Part A, **161**, 107094 (2022).
https://doi.org/10.1016/j.compositesa.2022.107094

[36] Plimpton S.: Fast parallel algorithms for short-range molecular dynamics. Journal of Computational Physics, **117**, 1–19 (1995).
https://doi.org/10.1006/jcph.1995.1039

[37] Müller-Plathe F.: Coarse-graining in polymer simulation: From the atomistic to the mesoscopic scale and back. ChemPhysChem, **3**, 754–769 (2002).
https://doi.org/10.1002/1439-7641(20020916)3:9<754::AID-CPHC754>3.0.CO;2-U

[38] Ries M., Steinmann P., Pfaller S.: Applying a generic and fast coarse-grained molecular dynamics model to extensively study the mechanical behavior of polymer nanocomposites: Dataset. Zenodo, Genève (2022). https://doi.org/10.5281/zenodo.6245701
[39] Evans D. J., Holian B. L.: The nose–hoover thermostat. The Journal of Chemical Physics, **83**, 4069–4074 (1985). https://doi.org/10.1063/1.449071
[40] Martyna G. J., Tobias D. J., Klein M. L.: Constant pressure molecular dynamics algorithms. The Journal of Chemical Physics, **101**, 4177–4189 (1994). https://doi.org/10.1063/1.467468
[41] Kremer K., Grest G. S.: Dynamics of entangled linear polymer melts: A molecular-dynamics simulation. The Journal of Chemical Physics, **92**, 5057–5086 (1990). https://doi.org/10.1063/1.458541
[42] Ries M., Dötschel V., Seibert J., Pfaller S.: A self-avoiding random walk algorithm (SARW) for generic thermoplastic polymers and nanocomposites. Zenodo, Genève (2022). https://doi.org/10.5281/zenodo.6245699
[43] Spannraft L., Ekh M., Larsson F., Runesson K., Steinmann P.: Grain boundary interaction based on gradient crystal inelasticity and decohesion. Computational Materials Science, **178**, 109604 (2020). https://doi.org/10.1016/j.commatsci.2020.109604
[44] Steinmann P., Runesson K.: The catalogue of computational material models: Basic geometrically linear models in 1D. Springer, Cham (2021). https://doi.org/10.1007/978-3-030-63684-5
[45] Haupt P.: Continuum mechanics and theory of materials. Springer, Berlin (2013). https://doi.org/10.1007/978-3-662-04775-0
[46] Pfaller S.: Discrete and continuous methods for modelling and simulation of polymer materials. Friedrich-Alexander-Universität Erlangen-Nürnberg, Erlangen (2021). https://doi.org/10.25593/opus4-fau-18036
[47] Treloar L. R. G.: The physics of rubber elasticity. Clarendon Press, Oxford (1975).
[48] Thompson A. P., Plimpton S. J., Mattson W.: General formulation of pressure and stress tensor for arbitrary many-body interaction potentials under periodic boundary conditions. The Journal of Chemical Physics, **131**, 154107 (2009). https://doi.org/10.1063/1.3245303
[49] Subramaniyan A. K., Sun C.: Continuum interpretation of virial stress in molecular simulations. International Journal of Solids and Structures, **45**, 4340–4346 (2008). https://doi.org/10.1016/j.ijsolstr.2008.03.016
[50] Savitzky A., Golay M. J.: Smoothing and differentiation of data by simplified least squares procedures. Analytical Chemistry, **36**, 1627–1639 (1964). https://doi.org/10.1021/ac60214a047
[51] Rubinstein M., Colby R. H.: Polymer physics. Oxford University Press, Oxford (2003).
[52] Liu S., Pfaller S., Rahimi M., Possart G., Steinmann P., Böhm M. C., Müller-Plathe F.: Uniaxial deformation of polystyrene-silica nanocomposites studied by hybrid molecular dynamics-finite element simulations. Computational Materials Science, **129**, 1–12 (2017). https://doi.org/10.1016/j.commatsci.2016.11.031
[53] Ndoro T. V., Voyatzis E., Ghanbari A., Theordorou D. N., Böhm M. C., Müller-Plathe F.: Interface of grafted and ungrafted silica nanoparticles with a polystyrene matrix: Atomistic molecular dynamics simulations. Macromolecules, **7**, 2316–2327 (2011). https://doi.org/10.1021/ma102833u
[54] Moghimikheirabadi A., Mugemana C., Kröger M., Karatrantos A. V.: Polymer conformations, entanglements and dynamics in ionic nanocomposites: A molecular dynamics study. Polymers, **12**, 2591 (2020). https://doi.org/10.3390/polym12112591
[55] Kröger M.: Shortest multiple disconnected path for the analysis of entanglements in two- and three-dimensional polymeric systems. Computer Physics Communications, **168**, 209–232 (2005). https://doi.org/10.1016/j.cpc.2005.01.020
[56] Shanbhag S., Kröger M.: Primitive path networks generated by annealing and geometrical methods: Insights into differences. Macromolecules, **40**, 2897–2903 (2007). https://doi.org/10.1021/ma062457k
[57] Karayiannis N. C., Kröger M.: Combined molecular algorithms for the generation, equilibration and topological analysis of entangled polymers: Methodology and performance. International Journal of Molecular Sciences, **10**, 5054–5089 (2009). https://doi.org/10.3390/ijms10115054
[58] Hoy R. S., Foteinopoulou K., Kröger M.: Topological analysis of polymeric melts: Chain-length effects and fast-converging estimators for entanglement length. Physical Review E, **80**, 031803 (2009). https://doi.org/10.1103/physreve.80.031803
[59] Kam K. M., Zeng L., Zhou Q., Tran R., Yang J.: On assessing spatial uniformity of particle distributions in quality control of manufacturing processes. Journal of Manufacturing Systems, **32**, 154–166 (2013). https://doi.org/10.1016/j.jmsy.2012.07.018
[60] Camesasca M., Kaufman M., Manas-Zloczower I.: Quantifying fluid mixing with the Shannon entropy. Macromolecular Theory and Simulations, **15**, 595–607 (2006). https://doi.org/10.1002/mats.200600037
[61] Hiemenz P. C., Lodge T. P.: Polymer chemistry. CRC Press, Boca Raton (2007). https://doi.org/10.1201/9781420018271
[62] Holzapfel G. A.: Nonlinear solid mechanics. Wiley, Chichester (2000).
[63] Bauer C., Ries M., Pfaller S.: Accelerating molecular dynamics simulations by a hybrid molecular dynamics-continuum mechanical approach. Soft Materials, in press (2022). https://doi.org/10.1080/1539445X.2022.2061513

[64] Zou H., Wu S., Shen J.: Polymer/silica nanocomposites: Preparation, characterization, properties, and applications. Chemical Reviews, **108**, 3893–3957 (2008). https://doi.org/10.1021/cr068035q

[65] Wang K., Wu J., Ye L., Zeng H.: Mechanical properties and toughening mechanisms of polypropylene/barium sulfate composites. Composites Part A: Applied Science and Manufacturing, **34**, 1199–1205 (2003). https://doi.org/10.1016/j.compositesa.2003.07.004

[66] Ou Y., Yang F., Yu Z-Z.: A new conception on the toughness of nylon 6/silica nanocomposite prepared *via in situ* polymerization. Journal of Polymer Science Part B: Polymer Physics, **36**, 789–795 (1998). https://doi.org/10.1002/(SICI)1099-0488(19980415)36:5<789::AID-POLB6>3.0.CO;2-G

[67] Ji X. L., Jing J. K., Jiang W., Jiang B. Z.: Tensile modulus of polymer nanocomposites. Polymer Engineering and Science, **42**, 983–993 (2002). https://doi.org/10.1002/pen.11007

[68] Mishra S., Sonawane S. H., Singh R. P.: Studies on characterization of nano $CaCO_3$ prepared by the *in situ* deposition technique and its application in PP-nano $CaCO_3$ composites. Journal of Polymer Science Part B: Polymer Physics, **43**, 107–113 (2004). https://doi.org/10.1002/polb.20296

[69] Douce J., Boilot J-P., Biteau J., Scodellaro L., Jimenez A.: Effect of filler size and surface condition of nanosized silica particles in polysiloxane coatings. Thin Solid Films, **466**, 114–122 (2004). https://doi.org/10.1016/j.tsf.2004.03.024

[70] Cho J., Joshi M. S., Sun C. T.: Effect of inclusion size on mechanical properties of polymeric composites with micro and nano particles. Composites Science and Technology, **66**, 1941–1952 (2006). https://doi.org/10.1016/j.compscitech.2005.12.028

[71] Blivi A. S., Benhui F., Bai J., Kondo D., Bédoui F.: Experimental evidence of size effect in nano-reinforced polymers: Case of silica reinforced PMMA. Polymer Testing, **56**, 337–343 (2016). https://doi.org/10.1016/j.polymertesting.2016.10.025

[72] Levita G., Marchetti A., Lazzeri A.: Fracture of ultrafine calcium carbonate/polypropylene composites. Polymer Composites, **10**, 39–43 (1989). https://doi.org/10.1002/pc.750100106

[73] Jarnthong M., Peng Z., Lopattananon N., Nakason C.: The influence of pre-compounding techniques and surface modification of nano-silica on the properties of thermoplastic natural rubber. Express Polymer Letters, **15**, 1135–1147 (2021). https://doi.org/10.3144/expresspolymlett.2021.92

[74] Prasad T., Halder S., Dhar S. S., Goyat M. S.: Epoxy/imidazole functionalized silica epoxy nanocomposites: Mechanical and fracture behaviour. Express Polymer Letters, **15**, 203–223 (2021). https://doi.org/10.3144/expresspolymlett.2021.19

[75] Sumita M., Shizuma T., Miyasaka K., Ishikawa K.: Effect of reducible properties of temperature, rate of strain, and filler content on the tensile yield stress of nylon 6 composites filled with ultrafine particles. Journal of Macromolecular Science Part B: Physics, **22**, 601–618 (1983). https://doi.org/10.1080/00222348308224779

[76] Rong M. Z., Zhang M. Q., Pan S. L., Lehmann B., Friedrich K.: Analysis of the interfacial interactions in polypropylene/silica nanocomposites. Polymer International, **53**, 176–183 (2004). https://doi.org/10.1002/pi.1307

[77] Hamdia K. M., Silani M., Zhuang X., He P., Rabczuk T.: Stochastic analysis of the fracture toughness of polymeric nanoparticle composites using polynomial chaos expansions. International Journal of Fracture, **206**, 215–227 (2017). https://doi.org/10.1007/s10704-017-0210-6

[78] Petrény R., Almásy L., Mészáros L.: Investigation of the interphase structure in polyamide 6–matrix, multiscale composites. Composites Science and Technology, **225**, 109489 (2022). https://doi.org/10.1016/j.compscitech.2022.109489

[79] Mészáros L., Deák T., Balogh G., Czvikovszky T., Czigány T.: Preparation and mechanical properties of injection moulded polyamide 6 matrix hybrid nanocomposite. Composites Science and Technology, **75**, 22–27 (2013). https://doi.org/10.1016/j.compscitech.2012.11.013

[80] Zhao W., Ries M., Steinmann P., Pfaller S.: A viscoelastic-viscoplastic constitutive model for glassy polymers informed by molecular dynamics simulations. International Journal of Solids and Structures, **226–227**, 111071 (2021). https://doi.org/10.1016/j.ijsolstr.2021.111071

[81] Zhao W., Steinmann P., Pfaller S.: A particle-continuum coupling method for multiscale simulations of viscoelastic–viscoplastic amorphous glassy polymers. International Journal for Numerical Methods in Engineering, **122**, 7431–7451 (2021). https://doi.org/10.1002/nme.6836

[82] Jain Y., Ries M., Pfaller S., Müller-Plathe F.: Addressing surface effects at the particle-continuum interface in a molecular dynamics and finite elements coupled multiscale simulation technique. Journal of Chemical Theory and Computation, **18**, 2375–2387 (2022). https://doi.org/10.1021/acs.jctc.1c00940

[83] Humphrey W., Dalke A., Schulten K.: VMD: Visual molecular dynamics. Journal of Molecular Graphics, **14**, 33–38 (1996). https://doi.org/10.1016/0263-7855(96)00018-5

[84] Kohlmeyer A., Vermaas J., Braun E.: Topotools. Zendolo, Genève (2020). https://doi.org/10.5281/zenodo.3845031